Monitoring methane gas migration in a near surface confined aquifer using electrical resistivity tomography

Timothy Cary, Rachel Lauer, and Kris Innanen

ABSTRACT

An 85% Methane composite gas was injected into a near surface confined aquifer at a rate of 1.5 m^3 per day, for 66 days from June 12th to August 16th, 2018. The field site, located in north-eastern British Columbia, is characterized as a fluvioglacial depositional environment which is consistent with the setting of the majority of energy wells in Alberta and British Columbia, Canada. 12 m of diamitic clay seal the injection target; a 14 m thick aquifer consisting of interbedded fine-grained sands and silts. Injection was focused at the base of the aquifer at 26 m depth. Electrical resistivity tomography (ERT), combined with distributed temperature sensing (DTS), was employed to monitor the migration and fate of the gas plume during and after the injection period. Three ERT lines were permanently installed for time lapse monitoring, two parallel and one orthogonal to groundwater flow (NW-SE), centered on or close to the injection location. Dipole-dipole and gradient arrays were employed on five occasions during injection and the data combined and inverted using RES2DINV to produce time lapse difference images. Results show resistivity increases of 15-25% near the injection zone. The gas plume is interpreted as spreading laterally until buoyancy driven preferential pathways are encountered to shallower depths. Resistivity increases of 15-25% are also seen at 10-12 m depth that coincide with gas flow observed at a monitoring well at 12m depth. DTS data were incorporated to correct the inversions for temperature effects. The general structure of the resistivity changes remains the same after temperature corrections are applied.

INTRODUCTION

The unintended release of natural gases, primarily comprised of methane, from well-bores is well documented. Boothroyd et al (2016) found that of 102 decommissioned onshore wells in the UK, 30% had significant increases in soil methane levels. Of 316,439 wells drilled in Alberta from 1910-2004, 4.6% were reported to have well integrity failures (Davies et al. 2014) creating the potential for fugitive gas migration. Methane poses risks as a greenhouse gas and as a contaminant in groundwater, which, if allowed to accumulate can create a potential explosion hazard. The shift in industry to hydraulic fracturing in recent years means that the volume of wells being drilled for unconventional resources has dramatically increased. Unconventional gas production in B.C. increased from 20% to 60% of B.C.'s total gas production from 2005 to 2012 (Rivard et al, 2014). Ingraffea et al (2014) reported in a Pennsylvania study that unconventional wells are between 1.57-6 times more likely to suffer from integrity failures than conventional wells, depending on the age of the well and the local geology. Therefore, as the unconventional sector continues to grow, there are likely to be more incidents of fugitive methane.

The migration and evolution of fugitive methane is less understood and is the key motivation for this paper. Developing a reliable and efficient monitoring strategy will reduce the risks posed by fugitive methane. The literature on subsurface monitoring of methane gas migration is limited. Steelman et al (2017) utilized time-lapse ground

penetrating radar (GPR) and ERT to monitor the migration of a methane gas plume in an unconfined sandy aquifer. The field experiment replicated a well-bore leak by injecting methane gas into the shallow subsurface. It was observed that the gas plume spread laterally when encountering vertical heterogeneities in grain size. Subtle variations in permeability caused by changes in the grain size direct the movement of the gas plume. Steelman also found that the gas was capable of moving much greater lateral distances than movement by groundwater advection alone. Numerical modelling of a controlled methane release was carried out by Klazinga (2018). Modelling showed that migration is primarily driven by buoyancy forces. Once the gas reaches a less permeable layer it spreads laterally until the pressure in the plume is great enough to break through the confining layer. GPR proved effective at locating the edges of the plume. ERT was able to image the main plume, however, it encountered difficulties when trying to image thin lateral migration pathways.

This study looks to expand this area of research into a heterogeneous geological environment similar to that of many of Canada's unconventional plays. The site, located near Fort St. John, B.C., is a fluvioglacial deposit located on the bluffs on the Peace River. The experiment utilizes time-lapse ERT combined with downhole DTS fiber in four wells to correct the data for temperature effects.

MULTIPHASE FLOW

Methane gas is not readily soluble in water at shallow subsurface pressures and temperatures (Cramer et al, 1999), thus the fluid dynamics in the pore space are that of multiphase flow of two immiscible fluids, water and methane gas. Here we are assuming that we are below the water table, therefore, the effective pore space is fully saturated with groundwater pre-injection. In order for the gas to move through the pore space it must displace the water that currently resides there. When the two fluids are in contact at a pore throat there is a pressure differential across the interface that connects them. This pressure differential is known as the capillary pressure (Bear, 2013)

$$P_c = P_{nw} - P_w \tag{1}$$

where P_{nw} is the pressure in the nonwetting fluid and P_w is the pressure in the wetting fluid. In our scenario methane gas is the nonwetting phase and water the wetting phase. Bear (2013) describes the capillary pressure as the tendency of a porous medium to repel the nonwetting phase. The capillary pressure is a function of the size of the pore throat, the smaller the pore throat the greater the capillary pressure. When the pore space is initially saturated with the wetting fluid (i.e. water) and is displaced by the nonwetting fluid (i.e. methane) it is called drainage (Bear, 2013). Before the nonwetting fluid can enter the pore and displace the wetting fluid a minimum pressure must be reached in the nonwetting fluid, known as the threshold pressure (Bear, 2013), which is equivalent to the capillary pressure. Threshold pressure is a function of the pore radius and proportional to grain size. Leverett (1941) showed that the capillary pressure is proportional to $1/\sqrt{k}$ where k is the permeability of the porous medium. Thus, a decrease in permeability results in a greater threshold pressure.

Thomson and Johnson (2000) put forth a conceptual model of an injected gas plume evolution, in their case air. Initially, the injection pressure will cause drainage of the pore space around the injection point, the pores fill with air. Buoyancy forces then dominate and

the gas begins to flow upwards. When the gas encounters a less permeable layer the threshold pressure to break into that medium becomes too great. At this point the plume begins to migrate laterally underneath the less permeable layer. At points where there are lateral heterogeneities in permeability the gas will again migrate upwards. This presents a mechanism for significant lateral migration of the gas plume in a vertically heterogeneous environment.

Given the laterally and vertically heterogeneous nature of our field site, it is predicted that the gas migration pathway will be extremely complex. The 12m thick clay layer that is pervasive across our site is likely to prevent gas from migrating into the vadose zone and ultimately into the atmosphere. The numerous monitoring wells onsite, although backfilled with bentonite, offer potential vertical pathways to surface. Lundegard and LaBrecque (1998) conducted an air sparge in a highly heterogeneous glacial till environment. Their results show significant lateral migration and a trapping of the plume below an assumed low permeability layer.

ELECTRICAL RESISTIVITY TOMOGRAPHY

Resistivity surveys are used to determine changes in subsurface resistivity in a noninvasive and nondestructive manner. A known current is injected into the ground and the potential measured between two electrodes along the current's path. Having a known current and measured potential allows one to calculate an apparent resistivity. Apparent resistivity measurements are inverted to create resistivity models for the site.

Electrical Theory

The method applies a continuous direct current into the ground between two electrodes and measures the potential at points between the current electrodes. The potential due to a point current source is given by

$$V = \frac{I\rho}{4\pi r} \tag{2}$$

where I is the injected current in Amperes, ρ is the resistivity of the medium in ohm meters, and r is the radial distance from the point source in meters (Telford, 1990). By moving this potential to the surface of the medium and assuming that air does not permit the flow of current equation 2 becomes

$$V = \frac{I\rho}{2\pi r} \tag{3}$$

the current flows radially away from the electrode creating hemispherical equipotential surfaces beneath the ground-air interface (Telford, 1990). For the field experiment we now introduce a second electrode such that the current flows into the ground via the first electrode and exits via the second. There are now two current potentials of equal magnitude and opposite polarity. The potential at a point is given by

$$V_1 + V_2 = \frac{I\rho}{2\pi}\left(\frac{1}{r_1} - \frac{1}{r_2}\right) \tag{4}$$

where r_1 is the radial distance from the first electrode and r_2 is the radial distance from the second electrode (Telford, 1990). ERT uses the potential difference between a pair of potential electrodes which leads to

$$\nabla V = \frac{I\rho}{2\pi}\left[\left(\frac{1}{r_1} - \frac{1}{r_2}\right) - \left(\frac{1}{r_3} - \frac{1}{r_4}\right)\right] \quad (5)$$

where r_3 and r_4 are the radial distances from the two current electrodes to the second potential electrode, and ∇V is the potential difference between the two potential electrodes. Equation 5 allows us to measure the apparent resistivity at different points in the subsurface (Telford, 1990). As the spacing between the electrodes increases the survey probes deeper into the subsurface. In general, the data collected are plotted in a pseudo section. The horizontal location of the resistivity measurement for symmetrical arrays is the center of the array. The data are given a pseudodepth, this is found by integrating the sensitivity function, the pseudodepth is located at the median depth of investigation (Loke, 2004)

Experimental Application

Two array types were used in this field experiment, the dipole-dipole array and the gradient array. The dipole-dipole array set up is shown in figure 1. The current electrodes (C1 and C2) are paired together and separated by a distance a, as are the potential electrodes (P1 and P2). The two pairs are then separated by a distance na, where n is an integer and is referred to as the expansion factor (Adepelumi et al, 2006). Figure 1 also shows how the acquired data are mapped to data levels depending on the expansion factor n. The horizontal location of the data point is the midpoint of the array. The pseudodepth assigned to the point is given by the median depth of investigation, which depends upon the value of n. Table 1 shows the median depth factors for different values of n that were used to calculate pseudodepths.

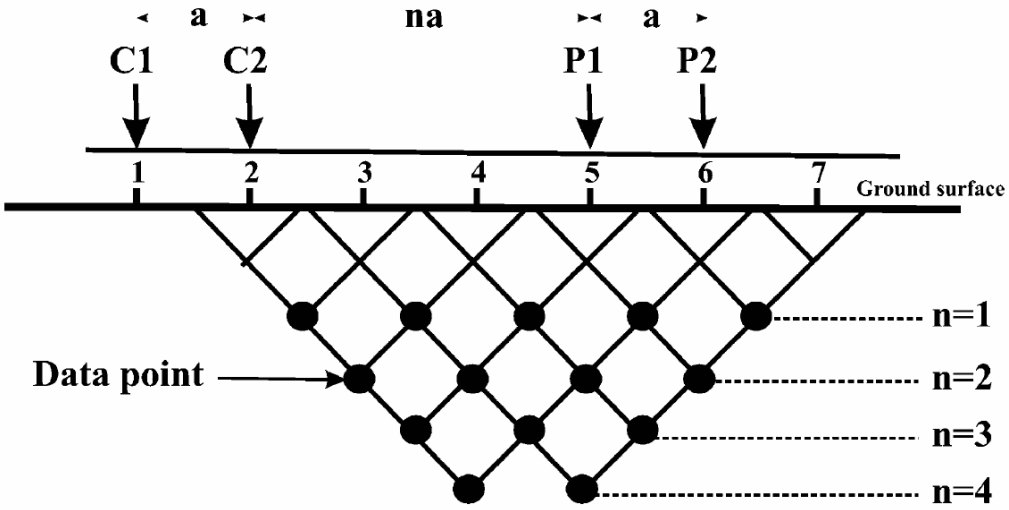

Fig. 1. Dipole-dipole array set up for field acquisition. C1 and C2 are the current electrodes, P1 and P2 are the potential electrodes. The separation of the electrode pair is a multiple n of the electrode spacing a. The data points below show how the acquired data map to data levels depending on the expansion factor n. (Adepelumi et al, 2006)

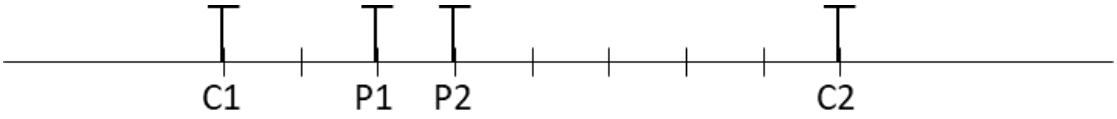

Fig. 2. Gradient array geometry. The current electrodes, C1 and C2, are kept at the ends of the survey. The potential electrodes, P1 and P2, move to each location between the current electrodes when recording data.

Array type		z_e/a	z_e/L
Dipole-dipole	n = 1	0.416	0.139
	n = 2	0.697	0.174
	n = 3	0.962	0.192
	n = 4	1.220	0.203
	n = 5	1.476	0.211
	n = 6	1.730	0.216
	n = 7	1.983	0.220
	n = 8	2.236	0.224

Table 1. Pseudodepth and geometric factors for a dipole-dipole array with different expansion factors (n). $\mathbf{z_e}$ is the pseudodepth, **a** is the electrode separation and **L** is the array length. Table adapted from Loke, 2004.

The gradient array set up is shown in figure 2. The two current electrodes, C1 and C2, are now at either ends of the array. The potential electrodes are moved to each location between the current electrodes. An estimate of the pseudodepth can be calculated by

$$z = min\{(x_{mid} - x_{C1}), (x_{C2} - x_{mid})\}/3 \qquad (6)$$

where x_{mid} is the midpoint of the potential electrodes P1 and P2, and x_{C1} and x_{C2} are the x locations of current electrodes C1 and C2 (Dahlin and Zhou, 2006).

Data Inversion

The data are inverted to produce resistivity models using RES2DINV ver 3.54.57. The inversion scheme used by the software is described by Loke (2004) and is as follows.

The inversion process looks to create a model of the desired parameter, in our case resistivity, based on the observed data in the field. RES2DINV creates a synthetic model response data set that is compared to the observed data and the difference between the two is minimized. The observed data in the field can be denoted as

$$\boldsymbol{d}_{obs} = [d_1, d_2, d_3, d_4, d_5, \dots, d_m] \tag{7}$$

where $d_m$is the m^{th} measurement. The model response is written as

$$\boldsymbol{d}_{est} = [D_1, D_2, D_3, D_4, D_5, \dots, D_m] \tag{8}$$

The model parameters are also shown in vector form as

$$\boldsymbol{q} = [q_1, q_2, q_3, q_4, q_5, \dots, q_n] \tag{9}$$

where n is the number of model parameters. The difference between the observed data and modeled data are given by

$$\boldsymbol{g} = \boldsymbol{d}_{obs} - \boldsymbol{d}_{est} \tag{10}$$

RES2DINV uses a least squares optimization method. Thus the model is adjusted each iteration to minimize the sum of squares error E

$$E = \boldsymbol{g}^T \boldsymbol{g} = \sum_{i=1}^{\boldsymbol{m}} g_{\boldsymbol{i}}^{\boldsymbol{2}} \tag{11}$$

The Gauss-Newton method is used to calculate the change in model parameters at each iteration

$$\boldsymbol{J}^T \boldsymbol{J} \Delta \boldsymbol{q} = \boldsymbol{J}^T \boldsymbol{g} \tag{12}$$

where $\Delta \boldsymbol{q}$ is the vector containing the changes in the model parameters, and $\boldsymbol{J}$ is the Jacobian matrix (m by n) of partial derivatives.

$$J_{ij} = \frac{\partial D_i}{\partial q_j} \tag{13}$$

Equation 13 denotes the change in the i^{th} model response to the change in the j^{th} parameter. The new model is given after the k^{th} iteration by

$$\boldsymbol{q}_{k+1} = \boldsymbol{q}_k + \Delta \boldsymbol{q}_k \tag{14}$$

The Gauss-Newton method of equation 12 is adjusted to the smoothness-constrained least-squares method presented by Ellis and Oldenburg (1994). This allows the inversion to deal with larger models with a large number of parameters, such as that of a 2D inversion, without producing erratic changes in resistivity. Equation 12 now becomes

$$(\boldsymbol{J}^T \boldsymbol{J} + \lambda \boldsymbol{F}) \Delta \boldsymbol{q} = \boldsymbol{J}^T \boldsymbol{g} - \lambda \boldsymbol{F} \boldsymbol{q} \tag{15}$$

where

$$\boldsymbol{F} = \alpha_x \boldsymbol{C}_x^T \boldsymbol{C}_x + \alpha_y \boldsymbol{C}_y^T \boldsymbol{C}_y + \alpha_z \boldsymbol{C}_z^T \boldsymbol{C}_z \tag{16}$$

and $\boldsymbol{C}_x$, $\boldsymbol{C}_y$ and $\boldsymbol{C}_z$ are the smoothing matrices in the x, y, and z directions with their corresponding weightings α_x, α_y, and α_z. This form of optimization also minimizes the square of the spatial changes, known as an l_2 norm smoothness-constrained optimization method.

RES2DINV also offers an l_1 norm smoothness constraint that minimizes the absolute changes in model resistivity values. This works well when the subsurface resistivity changes are not smooth and sharp contrasts between resistivity are expected. The method is known as the iteratively reweighted least-squares method (Wolke and Schwetlick, 1988). Equation 15 becomes

$$(\boldsymbol{J}^T\boldsymbol{J} + \lambda \boldsymbol{F_R})\Delta \boldsymbol{q} = \boldsymbol{J}^T \boldsymbol{R_d} \boldsymbol{g} - \lambda \boldsymbol{F_R} \boldsymbol{q} \tag{17}$$

where

$$\boldsymbol{F_R} = \alpha_x \boldsymbol{C}_x^T \boldsymbol{R_m} \boldsymbol{C}_x + \alpha_y \boldsymbol{C}_y^T \boldsymbol{R_m} \boldsymbol{C}_y + \alpha_z \boldsymbol{C}_z^T \boldsymbol{R_m} \boldsymbol{C}_z \tag{18}$$

where $\boldsymbol{R_d}$ and $\boldsymbol{R_m}$ are weighting matrices.

The model is made up of rectangular blocks of a fixed shape and size such that the model parameters are simply the resistivity values of each block.

Temperature Corrections

Electrical current in sedimentary structures flows through the pore fluid and by surface conduction on the grain surfaces (Hayley et al, 2007). Differences in conductivity due to temperature are caused by changes in viscosity in the pore fluid and ionic mobility at the grain surface (Hayley et al, 2007). Hayley et al (2007) conducted a laboratory experiment on glacial till samples and it was observed that from 0-25°C conductivity increases linearly with temperature. Haley's 2007 post-inversion method is applied here. The authors plan to use the more robust Haley et al. (2010) method in the near future, which incorporates the 2007 method, and is outlined as follows.

The first step is to run an inversion using RES2DINV. This produces a model of the subsurface resistivity $\boldsymbol{m}_{est}$ with the corresponding model response $\boldsymbol{d}_{est}$. The model is then corrected for temperature using the procedure from Hayley et al. (2007), producing a standard temperature equivalent model $\boldsymbol{m}_{est} + \Delta \boldsymbol{m}$ that has an associated model response $\boldsymbol{d}_{est}^{TC}$. To do this, the resistivity values $\boldsymbol{d}_{est}$ are converted to conductivity values as $\sigma = 1/\rho$ and the following equation from Haley et al. (2007) is applied

$$\sigma_{std} = \left[\frac{m(T_{std}-25)+1}{m(T_i-25)+1}\right] \sigma_i \tag{19}$$

where σ_{std} is the electrical conductivity at the standardized temperature, T_{std}, T_i is the in-situ temperature estimated from field data, σ_i is the in-situ conductivity taken from $\boldsymbol{d}_{est}$, and m is an empirically derived constant, which for our experiment will be 0.0183 °C^{-1}. We are using the same value as Haley et al. (2007) here due to the similarity between the soil samples of their experiment and our field site. $\boldsymbol{d}_{est}^{TC}$ is then calculated by forward modelling the newly temperature corrected model. The observed data are then temperature corrected by

$$\boldsymbol{d}_{obs}^{TC} = \boldsymbol{d}_{obs} + (\boldsymbol{d}_{est}^{TC} - \boldsymbol{d}_{est}) \tag{20}$$

The temperature corrected data can then be inverted to produce a final resistivity model.

DISTRIBUTED TEMPERATURE SENSING

Distributed temperature sensing is a method for collecting subsurface temperature data that utilizes fiber optic cables. The entire length of the fiber is capable of sensing temperature variations, enabling the continuous nature of the data. This offers considerable upside to single point measurements. The DTS used here relies on the Raman effect (Rogers, 1991). This is a quantum mechanical operation. Molecules within the silica fiber are vibrating depending on their temperature. A photon that is travelling down the fiber may be absorbed by a molecule, this raises the energy state of the molecule to a more excited state, the molecule will then spontaneously drop to a lower energy state, re-emitting a photon. If the molecule is already in an excited state, i.e. from having a higher temperature, the re-emitted photon can have greater energy than when absorbed, meaning a shorter wavelength (Rogers, 1991). The temperature along the fiber can be determined by analyzing the energy distribution of the backscattered light. The fiber is connected to an interrogator that pulses laser light down the fiber and records the backscattered light.

FIELD ACQUISITION

Site Description

The field site is located near Fort St John in north eastern British Columbia, Canada. The geological history of the area is a fluvioglacial environment. Core logs from monitoring wells show the site is glacial till, comprised of clay and silt down to 12 m. Under the clay are interbedded fine-grained sands to silts and silty clays to approximately 26 m, from 26-30 m is silty clay. The injection target is the base of the interbedded sand and silt zone from 12-26 m, a single screened injection well bore was drilled at a 45° angle to a total vertical depth of 26 m (Figure 3). Throughout the logs are many pebbles and cobbles between 1-10%. The site has little to no elevation change. Seven single screen monitoring wells and 13 multi-level wells; each containing four screens, were installed to a depth of 20 m (Figure 4). The weather throughout the injection was mostly hot and dry, interrupted by infrequent high intensity rainfall events; meaning the very near surface was often unsaturated. The water table decreased by approximately 30-50 cm from the NW well PW1 to the SE well PW4, suggesting a NW to SE groundwater flow direction. The water level varied from 2.37 m to 2.97 m in PW1 over the course of the injection period. An 85% methane composite gas mixture was injected at the field site between June 12th and August 16th, 2018. The injection rate was held constant at 1.5 m^3 per day for a total of 97.662 m^3.

Geophysical logging was recorded in the location of PW1 down to a depth of 70 m. An interpreted well log is shown in Figure 5. The dashed lines show the interpreted layers. Layer A ranges from 0 - 4.5 m and is comprised of soils and heterogeneous clayey silt diamict. The layer is characterized by high gamma counts of 75-105 API and a resistivity on the order of 10 Ω-m. Layer B ranges from 4.5 - 12 m and is clayey to silty diamict. It is characterized by gamma counts of approximately 60 API and resistivity on the order of 60 Ω-m, layers A and B act as the impermeable seal to the aquifer. Layer C goes from 12 - 23 m and is comprised of fine sand to silty diamict. The layer is characterized by gamma counts of approximately 45 API and resistivity on the order of 70-80 Ω-m, this is the main aquifer interval. Layer D ranges from 23 - 26 m and contains pebbly fine sand. The layer is characterized by gamma counts of approximately 40 API, a strong drop in the neutron

porosity count and variable resistivity between 30-100 Ω-m. Layers C and D are the intended injection target. Layer E ranges from 26 - 61 m and is comprised of silty, clay diamict. The layer is characterized by gamma counts of 75 API and a resistivity between 10 and 20 Ω-m. Layer F represents coarser material but is below the depth of this experiment.

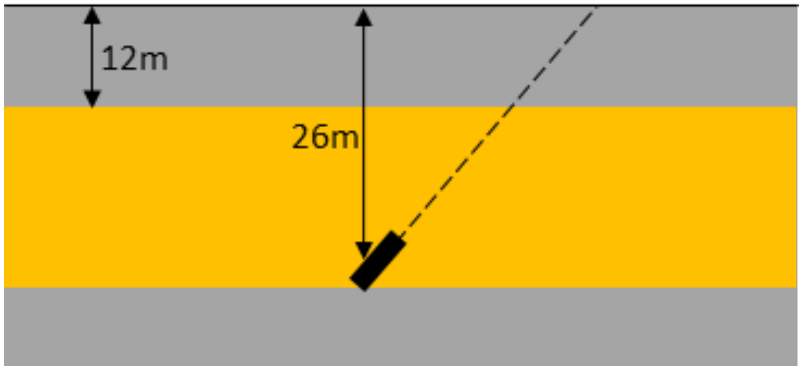

Fig. 3. Cross-sectional view of injection wellbore with sparging screen. The well was drilled to target the base of the sand aquifer at 26 m depth. The aquifer is sealed by approximately 12 m of clay/silt diamict. The grey layers indicate clay and silt dominated matrix and the yellow layer represents the fine-grained sand aquifer.

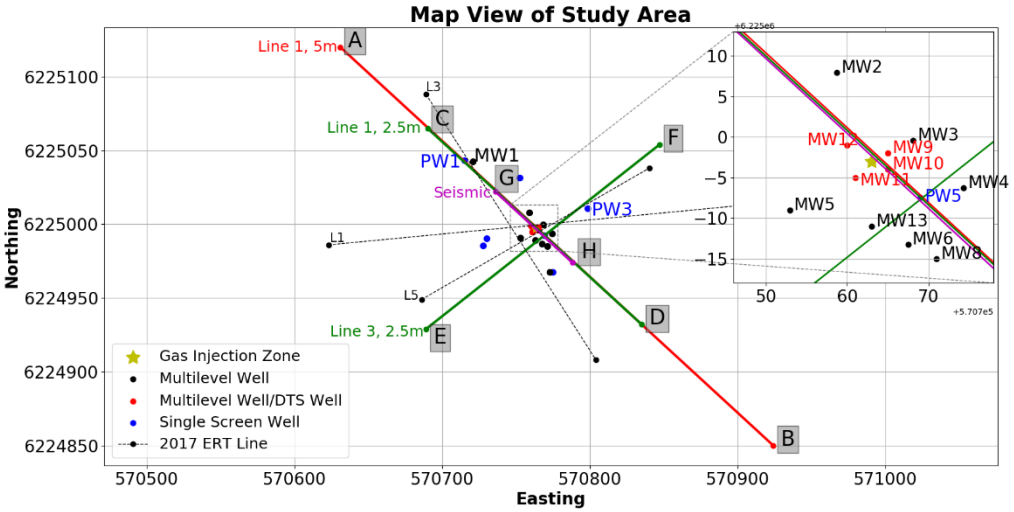

Fig. 4. Site map for methane gas injection

Electrical Resistivity Tomography

Three ERT lines were permanently installed with 81 12” electrodes per line to ensure that repeated measurements were in the same locations. The three lines are indicated in figure 4. There are two NW-SE lines that cross the injection location indicated from A to B and C to D. The two lines are differentiated by their electrode spacing. Line 1 from A-B has 5 m electrode spacing and line 1 from C-D has 2.5 m electrode spacing. Line 3 runs from E to F in a SW-NE orientation and has 2.5m electrode spacing. Line 3 intersects Line

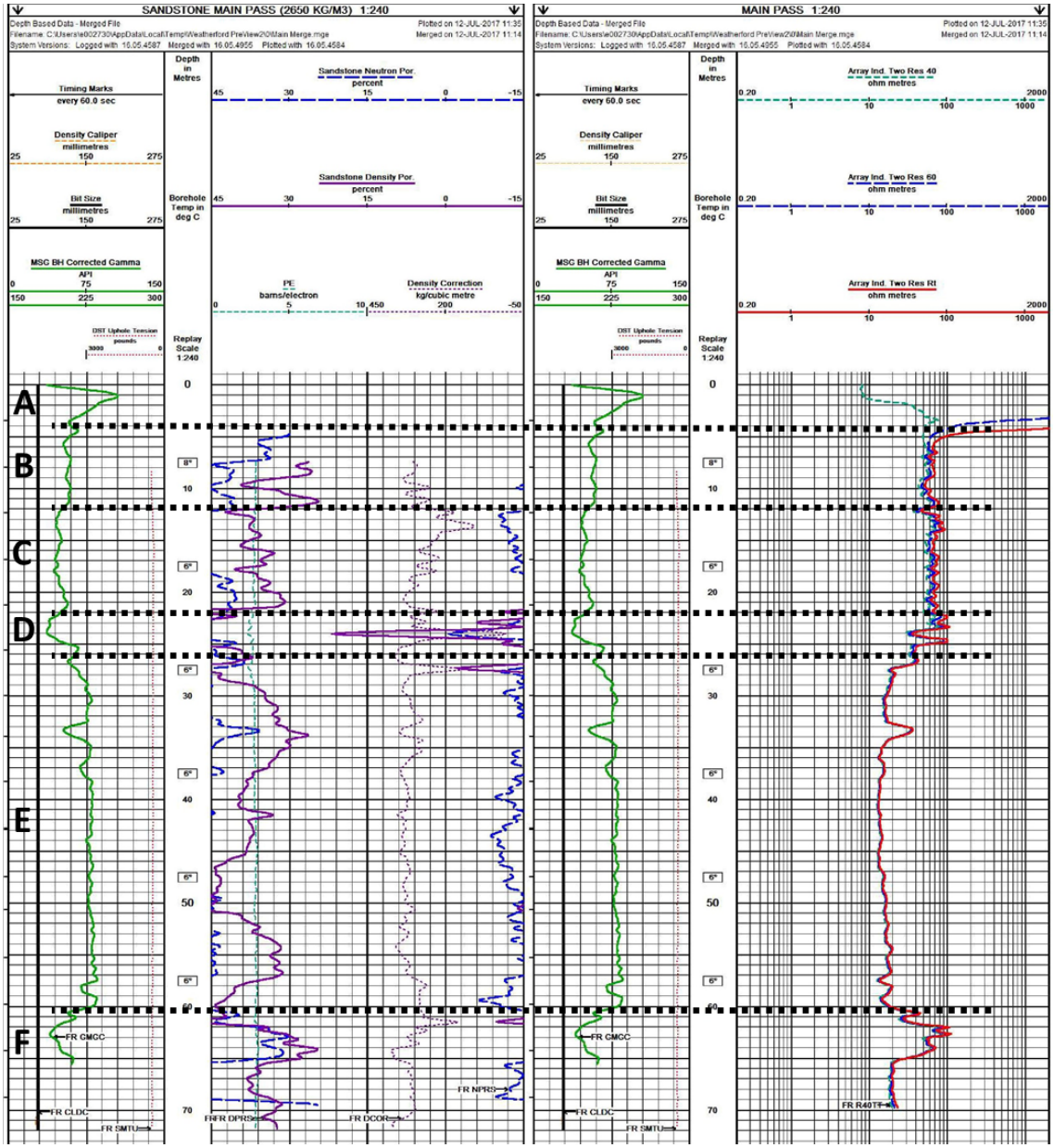

Fig. 5. Geophysical well logs from PW1. Dashed lines show interpreted layers. A (0 - 4.5 m): Soils to heterogeneous clayey silt diamict. Characterized by high gamma counts of 75-105 API. Resistivity on the order of 10 Ω-m. B (4.5 – 12 m): Clayey to silty diamict. Characterized by gamma of approximately 60 API and resistivity on the order of 60 Ω-m. C (12 – 23 m): Fine sand, silty diamict. Characterized by approximately 45 API and resistivity on the order of 70-80 Ω-m. D (23 – 26 m): Pebbly fine sand. Characterized by approximately 40 API, a strong drop in the neutron count and variable resistivity between 30-100 Ω-m. E (26 – 61 m): Silty, clay diamict: Characterized by gamma of 75 API and a resistivity between 10 and 20 Ω-m. F represents coarser material but is below the depth of investigation with the ERT lines.

1 at the observation well PW5. PW5 lies at the center of line 3. The injection point lies at the center of the 2.5 m spacing line 1.

The data were collected with the ABEM Terrameter LS 2. Data were collected during seven sessions from June 5th to September 27th. The numbering scheme used for data sets is days since the start of injection on June 12th. Line 1 (2.5 m and 5 m spacings) had data recorded on days 9, 23, 49, 61, 88, and 107. Line 3 had data recorded on days 9, 22, 49, 62, 89, and 107. Injection ceased on day 65, August 16th. A gradient array and a dipole-dipole array were collected on each day for each line.

Distributed Temperature Sensing

DTS fiber was installed into four wells, MW9, MW10, MW11, and MW12 (Figure 4). The depths of the wells are 21.34 m, 20.73 m, 20.88 m, and 20.73 m respectively. 2" diameter PVC pipe was installed into the borehole for the depth of the hole. The fiber was attached to metal spacers that were clamped to the PVC every 4 m to keep the fiber next to the borehole wall (Figure 6). This is required to keep the fiber thermally coupled to the formation. The boreholes were then backfilled with bentonite. The boreholes were also backfilled with one foot of sand around the water monitoring screens that were placed at the base of the borehole, and 2 m, 4 m, and 8 m from the bottom of the hole. The individual fiber loops for each well were installed separately and then fusion spliced together to form one large loop. The interrogator was installed on June 6th by Silixa and recorded measurements every hour until it was uninstalled on August 13th. The fiber had a spatial sampling interval of 0.25 m. Each data recording is the average temperature over a 15-minute period.

Fig. 6. Photograph showing how the DTS fiber was attached to the metal spacers to keep it flush with the borehole wall.

RESULTS

Different inversion parameters were tested on the baseline data to find a good match with the stratigraphic columns interpreted from the core logs (Figure 7). The inversion scheme used was a smoothness-constrained Gauss-Newton least squares method. A robust constraint was used on the data to minimize the effects of noise. A weak robust constraint was also used on the model resistivities to better model potential sharp boundaries at the edges of a gas plume. A few of the surveys had issues with equipment that caused erroneous data. These data were removed. The subsequent inversions had small values of absolute errors generally $< 2\%$, suggesting a good fit between the inversions and the data. The general structure of the models matches the well logs well. Inverted models from line 1 and line 3 show good agreement of resistivity values at their intersection (Figure 8). Figure 9 shows that there is a conductive layer at the top of the section (~30-40 Ωm) followed by a more resistive section that is interpreted to be the fine-grained sand aquifer between ~10-25m. The bottom of the section is a highly conductive clay layer (~10-20 Ωm) that is also seen in the well log from Figure 6 (Layer E). The models show significant lateral variations in resistivity and areas of higher resistivity within the upper 12 m that match the core logs. The top image of figure 12 shows that the fine-grained sand aquifer is not laterally continuous. The models indicate that the migration of the gas plume is likely extremely complex. The core logs in figure 7 also show clay layers within the sand aquifer which act as baffles to the upwards migration of gas. This creates an environment favorable to lateral migration of the gas plume.

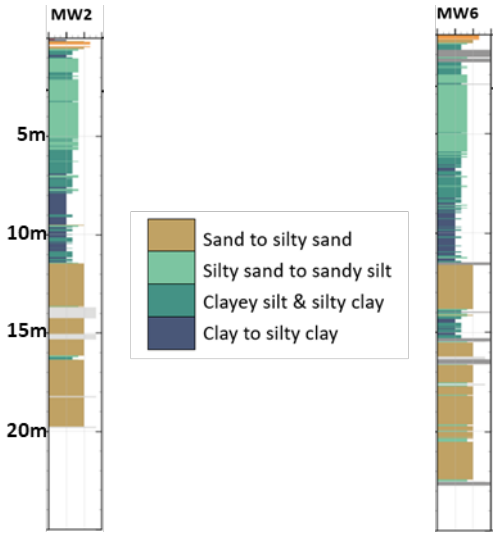

Fig. 7. Interpreted core logs from MW2 and MW6 show a thick clay layer above the sandy aquifer. There is also evidence of clay layers within the sand aquifer which act as baffles to the upwards migration of gas.

Figures 10, 11, and 12 show the percentage difference between the baseline model and the inverted model for four subsequent time data sets. The time lapse inversions were performed using the baseline model as the initial model for subsequent times. The inversions were carried out simultaneously using a constraint to minimize changes between the different time data sets and the reference model blocks. The inversion was regularized giving equal weighting to the data and the reference model. The data are poorly sampled

near the edges of the models and hence, changes near the edges are not interpreted as meaningful.

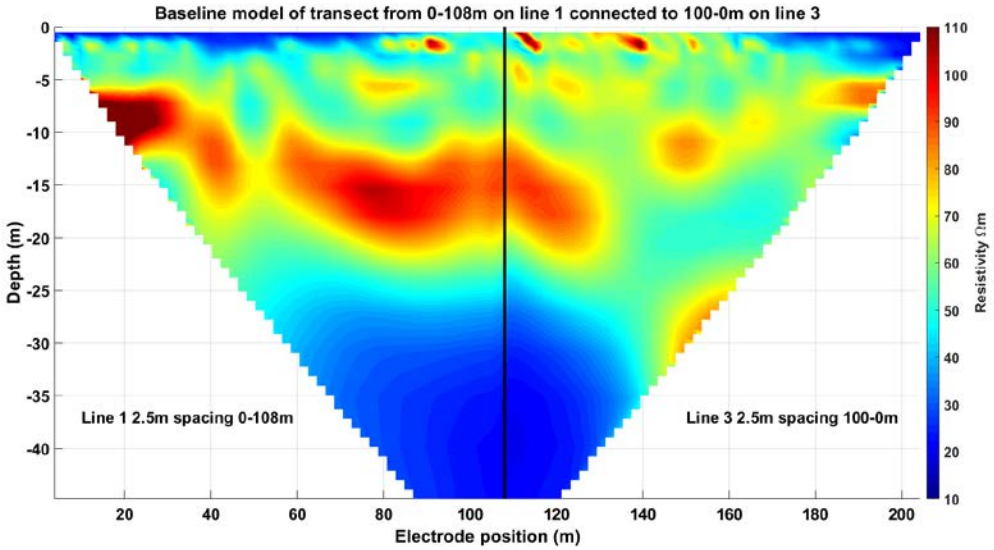

Fig. 8. Inversion models along a transect from 0-108 m on line 1 2.5 m spacing connected to line 3 at 100 m finishing at 0 m on line 3. Image shows good agreement between the inversions from the two different models at the intersection of the two lines.

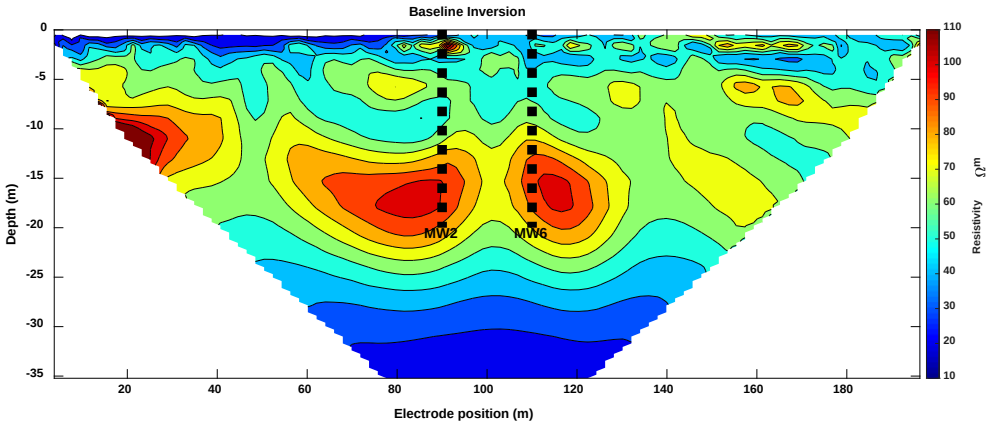

Fig. 9. Inversion of the baseline data for line 1 2.5 m spacing using a weak robust constraint. Inversion parameters were chosen as this data matched the core logs at MW2 and MW6, showing coarser grained sediment (high resistivity) at 5 m followed by clays and then sand.

Line 1 (2.5 m spacing) in figure 10 shows increases in resistivity near the injection point of up to 25%. The majority of the changes are seen below 20 m. Many of the core logs show layers of clay /silt within the fine-sand aquifer that would act as barriers to buoyancy driven migration. Hence, the gas would likely move laterally underneath such a layer until a lateral discontinuity in permeability offers a pathway to shallower depths. The June 21st image of figure 10 perhaps illustrates this mechanism. Free phase gas was detected at a monitoring screen from MW2 at 12 m depth, this is highlighted by the '+' sign. This coincides with an increase in resistivity of 25%. The gas may have migrated upwards from

the deeper section at this point. Once reaching this shallower depth, laterally pervasive increases in resistivity of up to 25% are seen. It is interpreted that the gas is again prevented from buoyancy driven migration by the 10-12 m clay layer at the top of the section and thus spreads laterally. The data from July 31st and August 12th support this picture of gas migration. The data from July 5th differ slightly, there are resistivity increases to the right of the injection and in the 10-12 m zone as before. However, the resistivity increases to the left of the injection point have gone. This may be due to some bad data points in that region or noise in the data. It might be possible that there was a disconnect in the plume that reconnects prior to the July 31st data set.

The 5 m spacing line 1 images in figure 11 have less resolution than the 2.5 m spacing images. As such it is difficult to interpret migration pathways in previous detail. What is evident is that there are resistivity increases around the injection point of up to 25%. The resistivity change increases in magnitude from June 21st to July 5th, decreases to July 31st and remains stable to August 12th. The decrease in resistivity change from 25% to 21% from July 5th to July 31st might be attributable to gas escaping to surface through MW2. Whilst testing water samples at MW2 the tap to the screen was open allowing gas to escape, which may have lowered the gas saturation in the pore space.

Line 3 in Figure 12 shows similar resistivity changes. Resistivity increases of up to 27% are seen around the injection point. Resistivity changes of up to 27% are also seen in in a thin layer around 10m depth, similar to line 1, this would be at the top of the aquifer, suggesting that the clay layer is confining the gas within the aquifer. Buoyancy driven migration again appears to be prevented around the injection point. It is interpreted that the gas spread laterally initially. Resistivity increases to the left of the injection point suggest upwards movement of the gas before the gas finds a pathway to the 10 m zone under the clay layer. The resistivity increase around the injection point increases in magnitude from 13% to 21% to 27% from June 21st through July 31st and remains constant at 27% for August 13th. This might suggest that the gas saturation increases from the start of injection and reaches a maximum around July 31st.

Figure 13 shows the data residuals stacked together for each line. This procedure reduces the effects of differences created by random noise in the data. Changes that are present throughout the time-lapse procedure will stack. We see that resistivity increases at the injection point and the monitoring screen have stacked in all three images. The magnitudes of these increases now greatly outweigh other changes present in the image. We cannot reduce all of the noise with only four difference images, but we create a better sense of the differences that are due to subsurface changes.

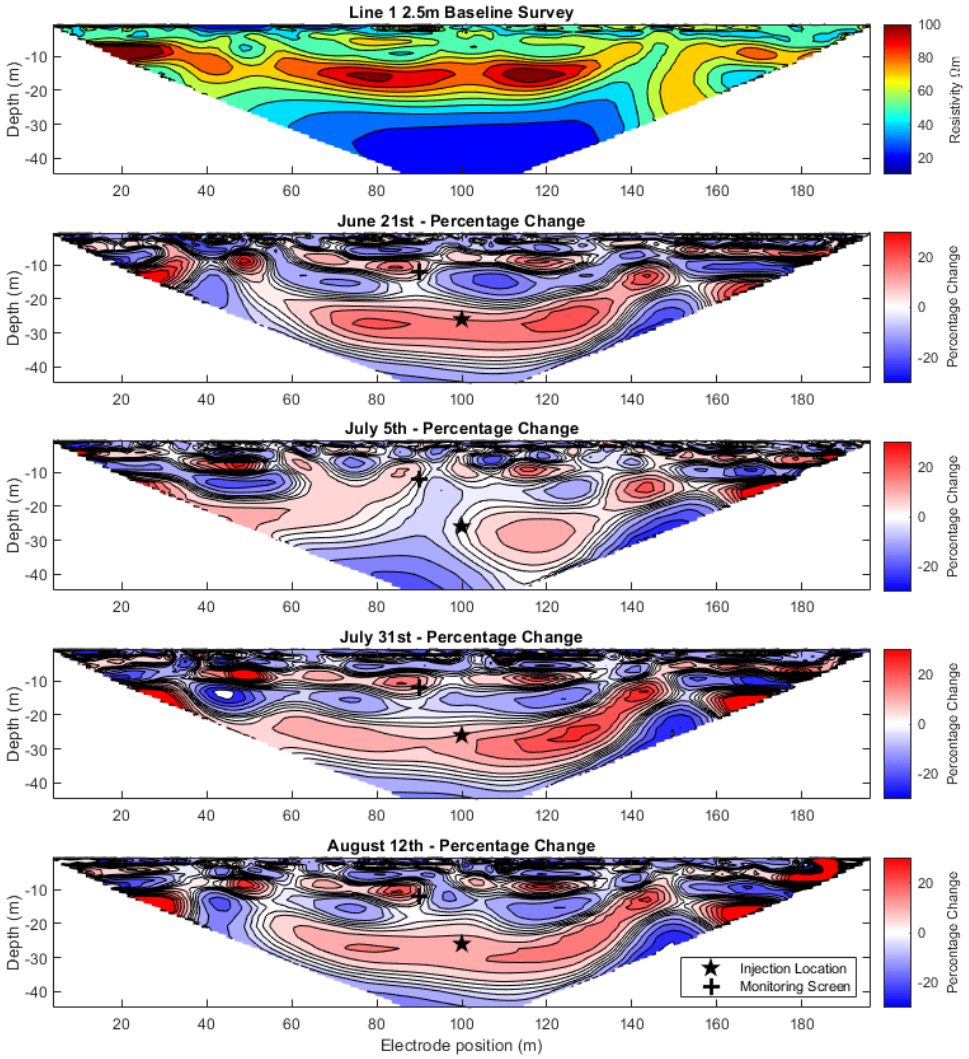

Fig. 10. Time-lapse ERT models for line 1 (2.5 m spacing) showing percentage changes relative to baseline model (Top). The injection location is indicated by the star at 26 m depth. Free phase gas was observed flowing from a monitoring screen at well MW2 ('+' symbol) at 12 m depth. Increases in resistivity near the injection point and the monitoring screen of up to 25% are interpreted to be a result of the presence of gas.

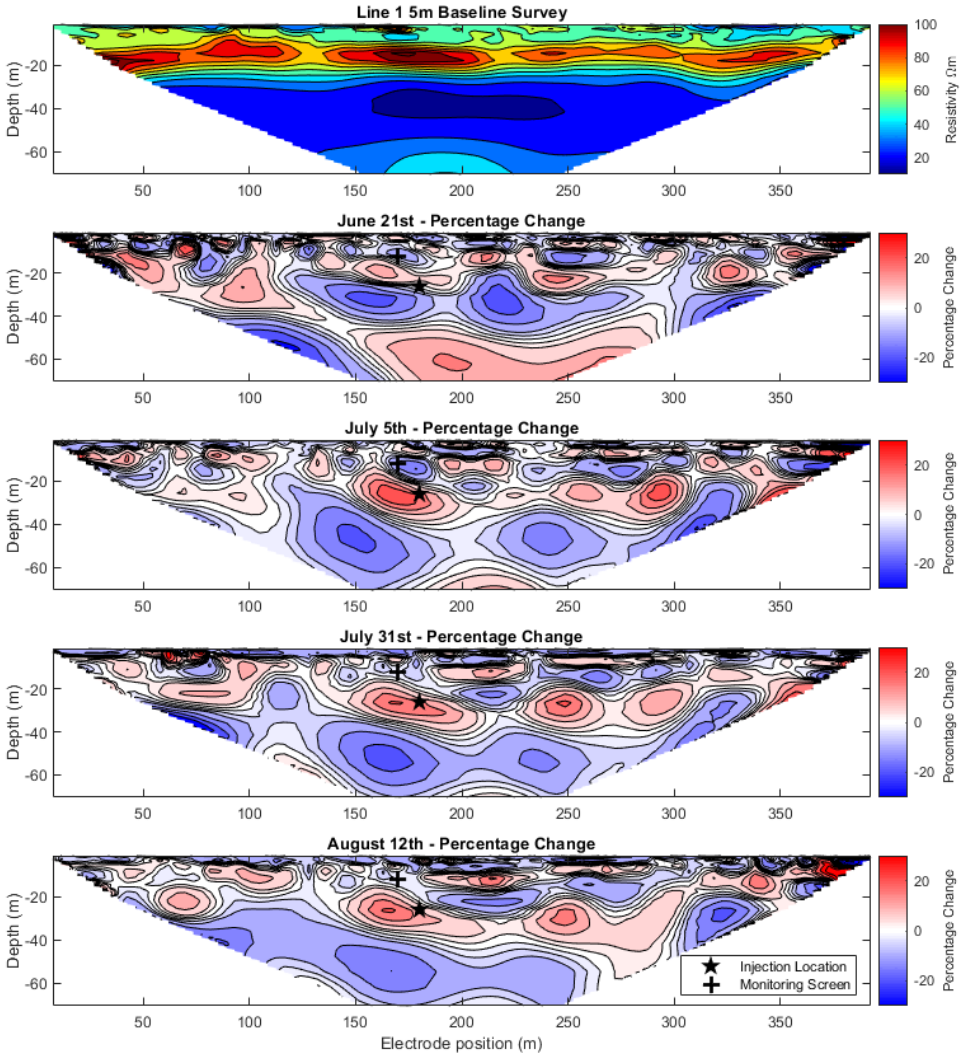

Fig. 11. Time-lapse ERT models for line 1 (5 m spacing) showing percentage changes relative to baseline model (Top). The injection location is indicated by the star at 26 m depth. Free phase gas was observed flowing from a monitoring screen at well MW2 ('+' symbol) at 12 m depth. Increases in resistivity near the injection point of 25% are interpreted to be a result of the presence of gas. The resistivity difference increases around the injection point from June 21st to July 5th. From July 5th to July 31st the resistivity increase drops from 25% to 21%, a potential cause for this is that gas escaped from well MW2 during water testing between the two ERT survey dates.

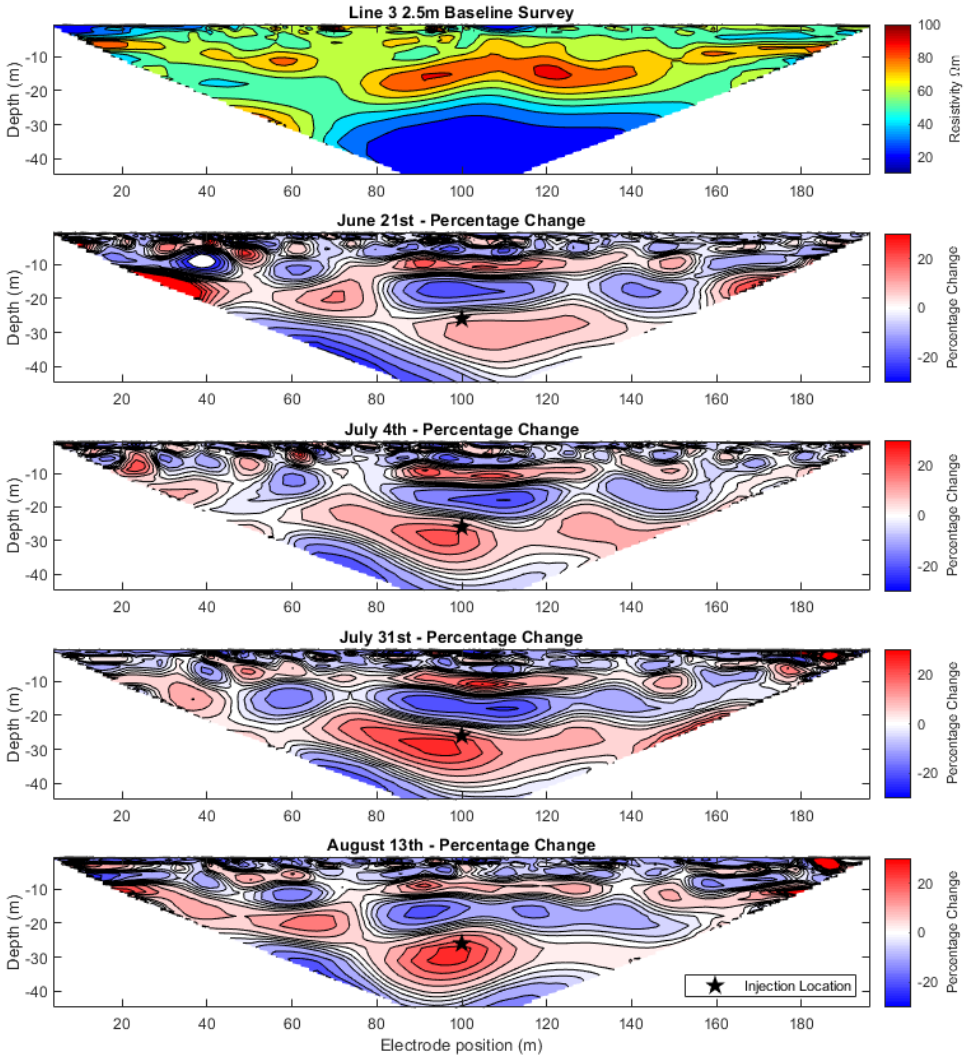

Fig. 12. Time-lapse ERT models for line 3 (2.5 m spacing) showing percentage changes relative to baseline model (Top). The injection location is indicated by the star at 26m depth. Increases in resistivity near the injection point of up to 27% are interpreted to be a result of the presence of gas. The resistivity difference increases from 13% to 21% to 27% from June 21st through July 31st. The resistivity increase remains at 27% from July 31st to August 13th. Resistivity increases of up to 27% are also seen under the clay layer at 10 m depth.

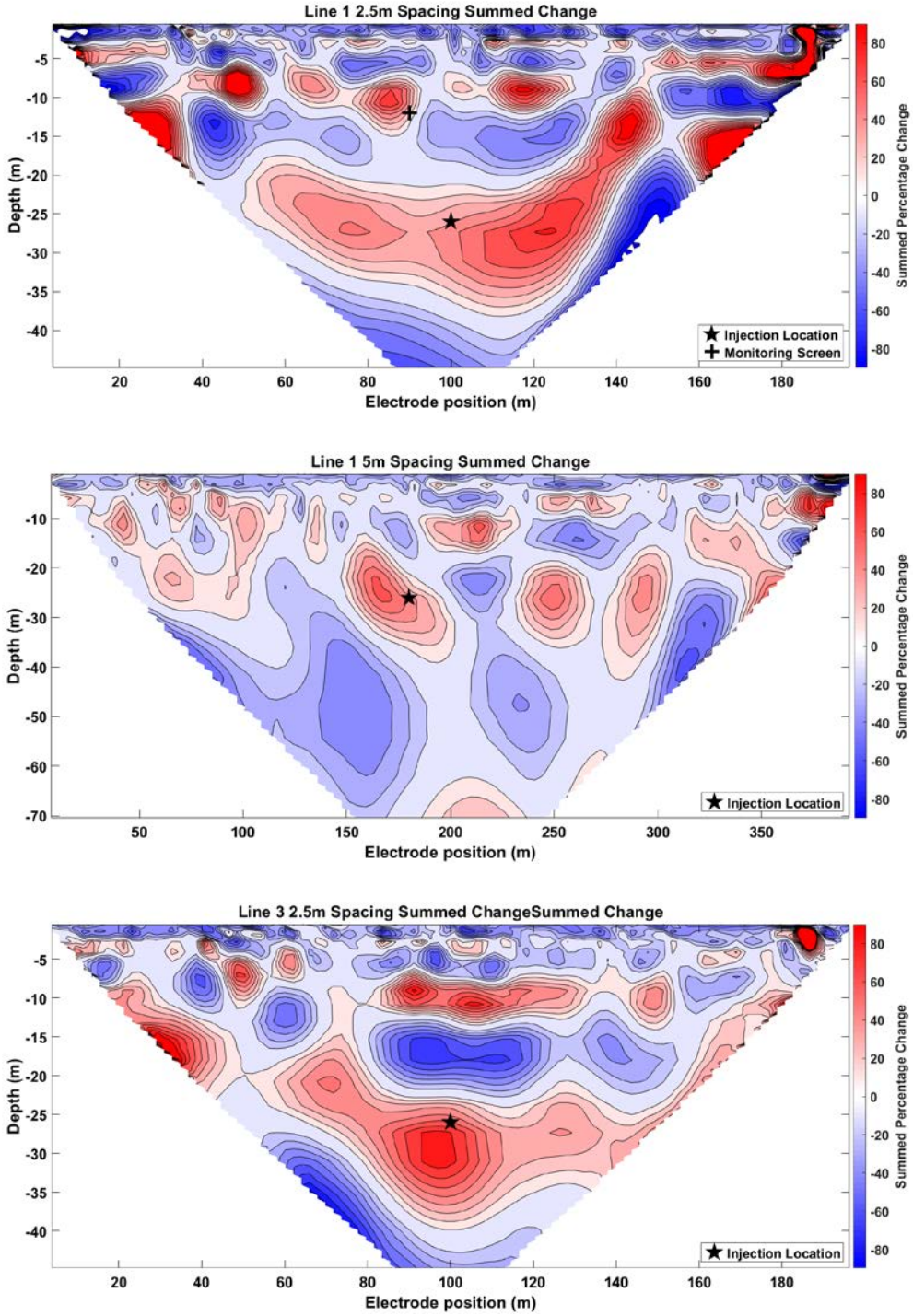

Fig. 13. The percentage differences for each of the data sets were summed to reduce noise in the images. We see strong stacking of increases in resistivity at our interpreted gas locations. The increases in resistivity are much larger in magnitude relative to other changes in the images.

CONCLUSIONS

Time-lapse ERT methods combined with monitoring well readings complement each other as to the migration and evolution of the injected methane gas in a heterogenous

confined aquifer. Injected methane causes an increase in resistivity around the injection zone, connected areas of resistivity increase are interpreted to gain insight on the migration of the gas plume. Resistivity increases of up to 27% are seen in areas of high confidence, i.e. the injection point and the monitoring screen where free phase gas was observed.

The injection zone at this site was extremely heterogeneous, containing many silty layers within the aquifer that act as baffles to the vertical buoyancy driven flow of methane. Difference images suggest mostly lateral movement of gas underneath these low permeability layers. The gas breaks through into shallower regions at lateral discontinuities of permeability and appears to pool under the 10-12 m thick clay layer that covers the site. Stacking of resistivity differences provides more confidence in the changes observed. Temperature corrections following the Haley et al. (2007) method reduce the decrease in resistivity seen in the near surface due to increases temperatures from the baseline survey.

FUTURE WORK

The more robust temperature correction method of Haley et al. (2010) will further remove changes that are not due to methane presence. This method corrects the data pre-inversion, this will not only correct near surface effects, but also deeper parts of the model, due to the aggregate nature of ERT survey readings.

REFERENCES

Adepelumi, A.A., Yi, M.J., Kim, J.H., Ako, B.D. and Son, J.S., 2006. Integration of surface geophysical methods for fracture detection in crystalline bedrocks of southwestern Nigeria. Hydrogeology Journal, 14(7), pp.1284-1306.

Bear, J., 2013. Dynamics of fluids in porous media. Courier Corporation.

Boothroyd IM, Almond S, Qassim SM, Worrall F, Davies RJ (2016) Fugitive emissions of methane from abandoned, decommissioned oil and gas wells. Sci Total Environ 547:461–469.

Cramer, B., Poelchau, H.S., Gerling, P., Lopatin, N.V. and Littke, R., 1999. Methane released from groundwater: the source of natural gas accumulations in northern West Siberia. Marine and Petroleum Geology, 16(3), pp.225-244.

Dahlin, T. and Zhou, B., 2006. Multiple-gradient array measurements for multichannel 2D resistivity imaging. Near Surface Geophysics, 4(2), pp.113-123.

Davies, R.J., Almond, S., Ward, R.S., Jackson, R.B., Adams, C., Worrall, F., Herringshaw, L.G., Gluyas, J.G. and Whitehead, M.A., 2014. Oil and gas wells and their integrity: Implications for shale and unconventional resource exploitation. Marine and Petroleum Geology, 56, pp.239-254.

Ellis, R.G. and Oldenburg, D.W., 1994. Applied geophysical inversion. Geophysical Journal International, 116(1), pp.5-11.

Hayley, K., Bentley, L.R., Gharibi, M. and Nightingale, M., 2007. Low temperature dependence of electrical resistivity: Implications for near surface geophysical monitoring. Geophysical research letters, 34(18).

Hayley, K., Bentley, L.R. and Pidlisecky, A., 2010. Compensating for temperature variations in time-lapse electrical resistivity difference imaging. Geophysics, 75(4), pp.WA51-WA59.

Ingraffea, A.R., Wells, M.T., Santoro, R.L. and Shonkoff, S.B., 2014. Assessment and risk analysis of casing and cement impairment in oil and gas wells in Pennsylvania, 2000–2012. Proceedings of the National Academy of Sciences, p.201323422.

Klazinga, D.R., 2018. Numerical investigation of the geophysical response to methane migration in an unconfined aquifer with implications for hydrocarbon wellbore leakage (Master's thesis, University of Waterloo).

Leverett, M., 1941. Capillary behavior in porous solids. Transactions of the AIME, 142(01), pp.152-169.

Loke, M.H., 2004. Tutorial: 2-D and 3-D electrical imaging surveys.

Lundegard, P.D. and LaBrecque, D.J., 1998. Geophysical and hydrologic monitoring of air sparging flow behavior: Comparison of two extreme sites. Remediation Journal, 8(3), pp.59-71.

Rivard, C., Lavoie, D., Lefebvre, R., Séjourné, S., Lamontagne, C. and Duchesne, M., 2014. An overview of Canadian shale gas production and environmental concerns. International Journal of Coal Geology, 126, pp.64-76.

Rogers, A.J., 1991, September. Distributed optical fiber sensing. In Chemical and Medical Sensors (Vol. 1510, pp. 2-25). International Society for Optics and Photonics.

Steelman, C.M., Klazinga, D.R., Cahill, A.G., Endres, A.L. and Parker, B.L., 2017. Monitoring the evolution and migration of a methane gas plume in an unconfined sandy aquifer using time-lapse GPR and ERT. Journal of contaminant hydrology, 205, pp.12-24.

Telford, W.M., Telford, W.M., Geldart, L.P., Sheriff, R.E. and Sheriff, R.E., 1990. Applied geophysics (Vol. 1). Cambridge university press.

Thomson, N.R. and Johnson, R.L., 2000. Air distribution during in situ air sparging: an overview of mathematical modeling. Journal of hazardous materials, 72(2-3), pp.265-282.

Wolke, R. and Schwetlick, H., 1988. Iteratively reweighted least squares: algorithms, convergence analysis, and numerical comparisons. SIAM journal on scientific and statistical computing, 9(5), pp.907-921.